Amplification of Brightness Variability by Active-region Nesting in Solar-like Stars

Emre Işık[1,2,3,5] , Alexander I. Shapiro[1] , Sami K. Solanki[1,4] , and Natalie A. Krivova[1]

[1] Max-Planck-Institut für Sonnensystemforschung, Justus-von-Liebig-Weg 3, D-37077 Göttingen, Germany; emre.isik@tau.edu.tr

[2] Department of Computer Science, Turkish-German University, Şahinkaya Cd. 108, Beykoz, 34820 Istanbul, Turkey

[3] Feza Gürsey Center for Physics and Mathematics, Boğaziçi University, Kuleli, 34684 Istanbul, Turkey

[4] School of Space Research, Kyung Hee University, Yongin, Gyeonggi-Do, 446-701, Republic Of Korea; solanki@mps.mpg.de

Abstract

Kepler observations revealed that hundreds of stars with near-solar fundamental parameters and rotation periods have much stronger and more regular brightness variations than the Sun. Here we identify one possible reason for the peculiar behavior of these stars. Inspired by solar nests of activity, we assume that the degree of inhomogeneity of active-region (AR) emergence on such stars is higher than on the Sun. To test our hypothesis, we model stellar light curves by injecting ARs consisting of spots and faculae on stellar surfaces at various rates and nesting patterns, using solar AR properties and differential rotation. We show that a moderate increase of the emergence frequency from the solar value combined with the increase of the degree of nesting can explain the full range of observed amplitudes of variability of Sun-like stars with nearly the solar rotation period. Furthermore, nesting in the form of active longitudes, in which ARs tend to emerge in the vicinity of two longitudes separated by 180°, leads to highly regular, almost sine-like variability patterns, rather similar to those observed in a number of solar-like stars.

Unified Astronomy Thesaurus concepts: G dwarf stars (556); Solar analogs (1941); Stellar activity (1580); Starspots (1572)

1. Introduction

Rotational brightness variability of Sun-like stars results from the transit of stellar magnetic features, i.e., dark spots and bright faculae, over the visible stellar hemisphere. The advent of high-precision photometry brought by planet-hunting missions allowed measuring rotational variability for several hundred thousands of stars (Basri et al. 2013; Reinhold et al. 2013; Walkowicz & Basri 2013; McQuillan et al. 2014). It also took solar–stellar connection studies to a new level, by allowing solar variability to be compared with that of solar peers.

Recently, Reinhold et al. (2020, hereafter R20) identified 2529 stars with near-solar fundamental parameters, but with unknown rotation periods (hereafter pseudosolar stars) and 369 stars with near-solar rotation periods and near-solar fundamental parameters (hereafter solar-like stars). While many of the pseudosolar stars are expected to have near-solar rotation periods, the sample most probably also includes stars with different periods (in particular, stars rotating slower than the Sun). The light curves of pseudosolar stars appear rather irregular, often resembling the solar light curve, and their variability amplitudes lie mostly within the solar range. Consequently, the Sun appears to be a typical star belonging to the pseudosolar sample: it would most probably be attributed to this sample if observed by Kepler, owing to difficulties in determining its rotation period.

Surprisingly, the variability pattern of solar-like stars differs from that of the pseudosolar stars and the Sun. First, R20 found that the mean variability in their solar-like sample was 5 times stronger than solar variability. Second, many of the stellar light curves had a rather regular temporal profile, often resembling a sine wave. This is in stark contrast to the Sun, which has a complex and quite irregular light curve. Especially at periods of high magnetic activity the solar light curve becomes so irregular that even the solar rotation period cannot be determined correctly from photometry, using standard methods like the autocorrelation function and Lomb–Scargle periodograms (see, e.g., Aigrain et al. 2015; Amazo-Gómez et al. 2020; Witzke et al. 2020).

We illustrate the difference between the variability of the Sun and solar-like stars in Figure 1, where we compare the Kepler light curve of KIC 7019978 ($T_{\rm eff} = 5726$ K, $P_{\rm rot} = 26.76$ days) with that of the Sun during the maximum of Cycle 23. The solar light curve as it would be observed in the Kepler passband has been taken from Nèmec et al. (2020). The strong dip in the solar light curve ($t \sim 2950$ days) was caused by a rather unusual configuration of magnetic features on the solar surface: three very large active regions (ARs) on one longitudinal hemisphere (i.e., within a longitudinal extent of 180°) had emerged contemporaneously, while the opposite hemisphere remained free of ARs. Single dips of such depths occur rarely in the solar brightness variations. The remaining shallower dips represent the typical effect of sunspot groups around activity maximum. The rotational brightness modulation of KIC 7019978 is clearly more vigorous and much more regular than that of the Sun, which varies its brightness on a comparable level only during the transit of that extraordinary concentration of three very large ARs.

All in all, the R20 study raised an intriguing question: how can large-amplitude and regular light curves of solar-like stars be produced and, in particular, what is the difference between the surface magnetism of the Sun and of solar-like stars? We introduce here two potential hypotheses for explaining the difference between the Sun and solar-like stars: (i) the surface coverage of magnetic features is larger than typical solar levels, leading to higher variability; (ii) the longitudinal distribution of magnetic features is more clumpy than on the Sun, leading to an amplification of brightness variations for a given level of magnetic flux or activity.

---

[5] Current address: Dept. of Computer Science, Turkish-German University, Istanbul, Turkey.
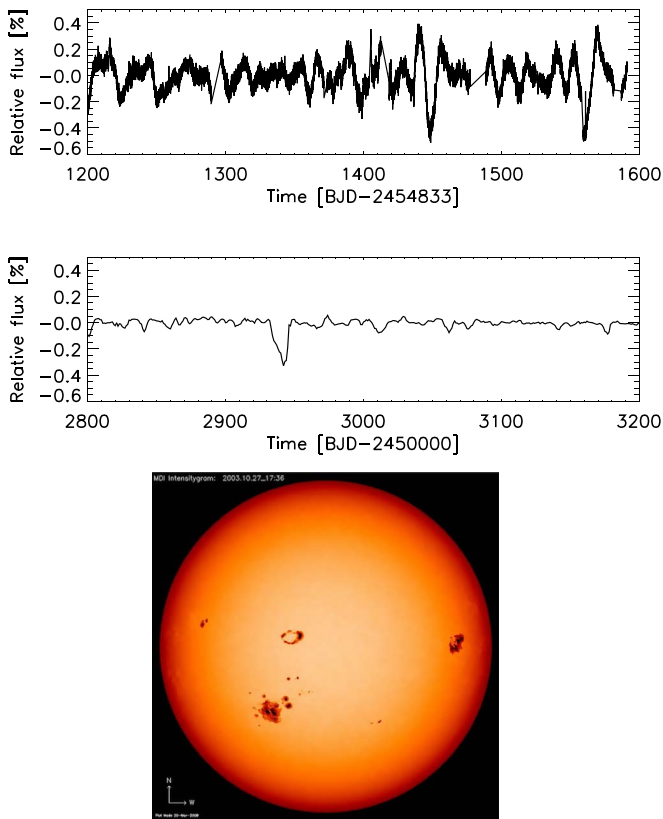
Figure 1. Brightness variations of KIC 7019978 (top panel) and of the Sun (middle panel), plotted on the same scale of the vertical axis. The SOHO/MDI image (bottom panel) corresponds to the time of the exceptionally strong dip in the solar light curve above, around 2940 days. Note the conspicuous differences in shape and amplitude of the variations of the two stars.

The first hypothesis is supported by the fact that solar cycles can have different strengths. For example, cycle 19 was stronger than Cycle 24 by a factor of 3 to 4 in terms of the maximum average sunspot number. One can speculate that the dynamos of solar-like stars can produce cycles at a wider range of strengths than those of the Sun, although it is a priori unclear why this should be so.

The second hypothesis is motivated by the tendency of solar ARs to emerge into regions of recent magnetic flux emergence, called complexes or nests of activity (Gaizauskas et al. 1983; Castenmiller et al. 1986; Brouwer & Zwaan 1990; Usoskin et al. 2005). The exact physical mechanisms for AR nesting are as yet unclear. The weak rotational variability and the irregular light variations of the Sun (and pseudosolar stars with undetermined rotation periods) could be related to the low degree of active-region nesting (e.g., only 40%–50% of sunspots are associated with nests; see Pojoga & Cudnik 2002). On solar-like stars with high variability and regular light curves, magnetic flux emergence can be clustered to higher degrees than on the Sun. The effects of AR nesting on photometric variability has not been studied to date. Here we present a simple model that quantifies the effects of nesting on photometric variability of solar-like stars in the Kepler passband for a range of magnetic activity levels.

2. Method

2.1. Modeling Brightness Variations

To simulate stellar light curves, we employ the model developed by Shapiro et al. (2020a). We simulate brightness variations of a solar-like star as observed equator-on (inclination $i = 90°$) for a period of 4.4 yr (close to Kepler's operation time) with a sampling rate of four measurements per day. Different activity levels are obtained by letting different numbers of ARs (consisting of spot groups and faculae) emerge within the latitude limits $\pm30°$, assuming a size distribution of ARs as on the Sun (i.e., a log-normal function; Bogdan et al. 1988; Baumann & Solanki 2005). The AR emergence frequency depends on the activity level, but for a given activity level it is constant in time, so that we do not consider any systematic change in the activity level during the simulated period. Following the approach of Shapiro et al. (2020a), we use solar dependences of facular and spot disk coverages on the chromospheric S-index (given by Equations (1)–(2) from Shapiro et al. 2014). We thus quantify the activity level in terms of S, which is taken as an average over the simulated time range. We consider a linear (in time) decay law of active regions and fixed the ratio between the lifetime of facular and spot parts of ARs to three. A more detailed description of light-curve modeling is given in the Appendix.

To measure variability, we split the entire light curve into 90 day segments (to be compatible with Kepler quarters), calculate the peak-to-peak variability in each of them, and take the mean value among the segments, which we call R_{90}. We consider peak-to-peak variability instead of the 95% to 5% difference often employed in the literature (e.g., Basri et al. 2013, R20), because our simulated light curves are free of noise.

2.2. Nesting Active Regions

To simulate nests of ARs, we consider two distinct modes. In the *free-nesting* mode, clusters of magnetic features form and decay sequentially. An active region (AR) emerges either (a) in the vicinity of the previous emergence location with a fixed probability p, or (b) at a random location within the latitude range of $\pm30°$ with the remaining probability $1-p$. The procedure is very similar to the one introduced by Işık et al. (2018, see their Appendix C). The proximity of an AR's emergence location to the nest center is drawn from a two-dimensional Gaussian process with standard deviations of $2°$ in latitude and $3°$ in longitude, which closely represent the observational values given by Pojoga & Cudnik (2002). The algorithm is designed in such a way that multiple nests can form sequentially, not contemporaneously. This means that before all the members of a given nest have fully emerged, a new nest does not begin to form. The development of a nest is thus completed when the subsequently emerging AR does not belong to the nest. However, a new nest can start to form when an existing nest (or nests) have not fully decayed, owing to size-dependent lifetimes of constituent spots and faculae.

In the *double active-longitude* (AL) mode, the probabilistic procedure is the same as for the free-nest mode, but ARs tend to emerge near one of the two "active" longitudes separated by 180° (with equal probability). The proximity of an AR to its host active-longitude is set randomly, using a normal distribution with $\sigma = 10°$ in longitude.
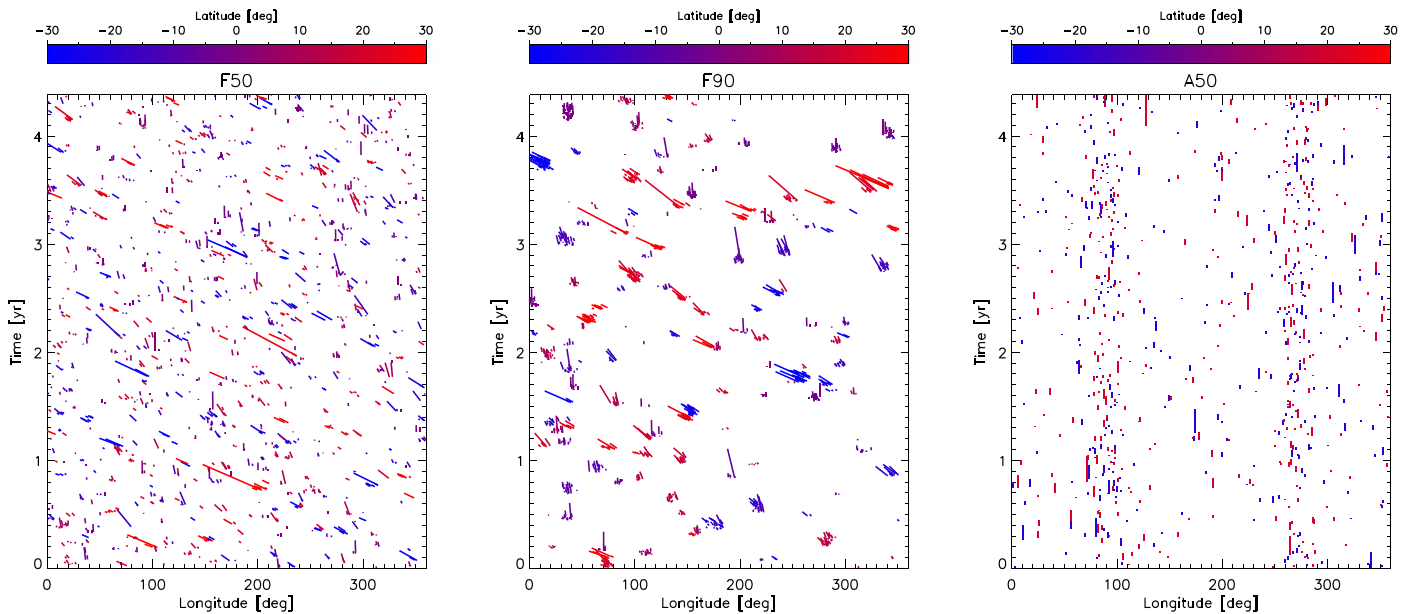
Figure 2. Time–longitude maps of active-region occurrence for an activity level close to that of a typical solar maximum, $S = 0.182$. The panels show the nesting modes F50, F90, and A50, from left to right (see the main text for definitions). Colors denote AR latitudes. The vertical extension of each element represents the spot-group lifetime for the corresponding AR.

In both nesting modes we set the probability p of a given AR to be associated to a nest (whether a free-nest or AL) as a free parameter. In the following, we will use the notations FP and AP, where the prefix describes the nesting mode (F for free nesting and A for AL), and P stands for the percentile probability of a given AR to emerge as part of a nest.

In the free-nesting case, the nest centers, as well as ARs emerged inside or outside of nests follow the solar surface differential rotation over latitude λ (Snodgrass 1983):

$$\Omega'(\lambda) = -2.3 \cos^2 \lambda - 1.62 \cos^4 \lambda, \qquad (1)$$

where $\Omega' = \Omega(\lambda) - \Omega(0)$ is the rate at which spots drift in longitude (in the equatorial rest-frame).

On the Sun, ALs are detected only in a dynamical reference frame, synchronized with the latitude-dependent rotation periods of major flux emergence regions (Usoskin et al. 2005). Even if we assume an initially coherent AL, differential rotation would destroy this pattern in only a few stellar rotations. Taking a rigid AL and applying differential rotation to individual ARs on smaller scales would have only a minor effect on the variability. To keep our model simple, we thus opted for rigid rotation in the AL mode, to compute brightness variations for an extremely coherent mode of nesting, because our goal is to assess the entire potential variability range.

Figure 2 shows the locations and lifetimes of spot groups for models F50, F90, and A50, for $S = 0.182$, typical of a solar maximum. Longer lifetimes are associated with larger spot groups, in agreement with the Gnevyshev–Waldmeier rule of sunspot groups. From F50 to F90 there is a dramatic increase in the degree of clustering of spot groups, which is expected to amplify photometric variability. Also the A50 case demonstrates significant clustering in longitude. In the F50 and F90 cases the differential rotation leads spot groups and free nests to exhibit longitudinal drifts at rates depending on the latitude (see, e.g., Özavcı et al. 2018).

3. Results

3.1. Nesting Amplifies Variability

We first investigate the dependence of the photometric variability on the level of magnetic activity for different modes and degrees of nesting. Since we are interested in finding the upper limit of variability, we only performed simulations for stars observed from their equatorial planes. Solar-like stars observed from out of this plane will show smaller variabilities (Nèmec et al. 2020). We carried out 10 random realizations of AR emergences for each combination of activity level and degree of nesting, with the exception of 50 realizations for F100. Such multiple runs were made to quantify the posterior width owing to randomness in AR emergence.

Figure 3 shows R_{90} as a function of S for free-nesting and active-longitude modes. Variability increases with S in all cases, owing to an increasing occurrence of ARs (which depends on the S; see Section 2). For F00 (i.e., for random emergence locations), R_{90} scales roughly linearly with S. The dependences for higher degrees of nesting gradually deviate from linearity with increasing S. This is because the area coverage of spots is proportional to S^2 in the model, in accordance with solar data. A random distribution of spots would thus imply that the variability is proportional to the square root of spot coverage, i.e., to S. Stronger nesting steepens the dependence and in the extreme case of 100% nesting the variability is proportional to the coverage, i.e., to S^2.

Comparison of the left and right panels of Figure 3 shows that the AL mode enhances variability even more than free nesting. This is because the permanent active longitudes lead to a more coherent superposition of ARs during each full rotation. Starting from A50, the dependences are nearly quadratic, in parallel with the functional relationship between the spot coverage and S.

In their sample of solar-like stars, R20 detected variability amplitudes of up to 0.7%. Taking $R_{90} = 0.7\%$ as an upper limit, we can consider various possibilities for how such a
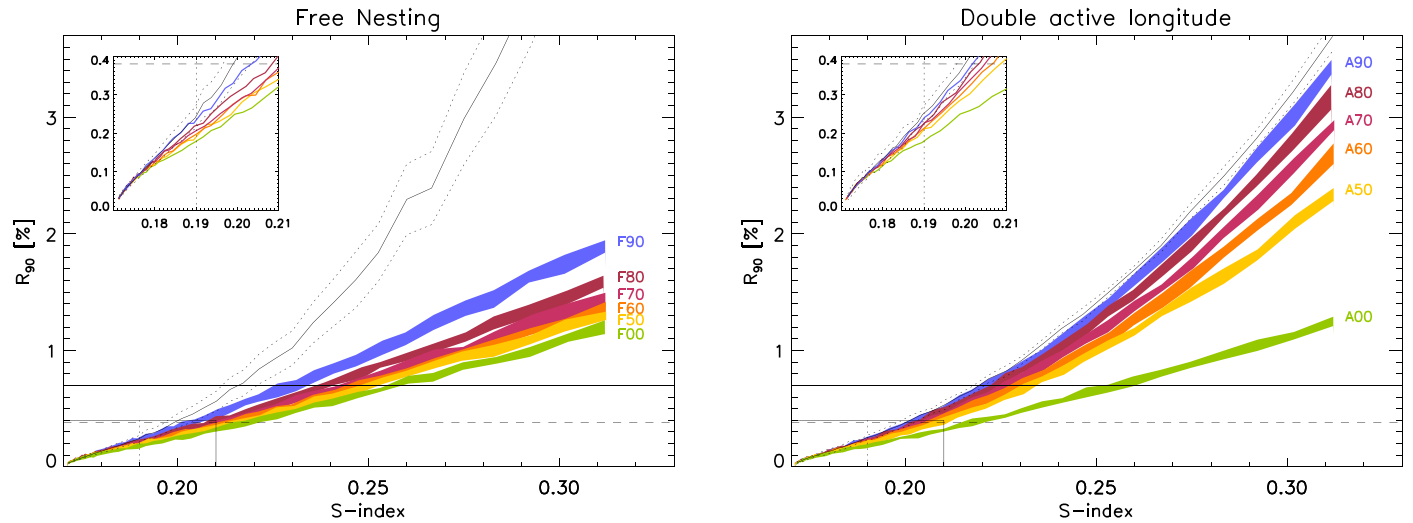
Figure 3. Mean amplitudes of rotational variability as a function of S for free nesting (left) and active longitudes (right), for a set of nesting degrees indicated by different colors. The vertical thickness of each colored band represents the $\pm 1\sigma$ scatter in R_{90} for a set of 10 random realizations (for F100, 50 realizations were used). The standard deviation in S is of order 10^{-4}. The black curves show the case of 100% nesting (F100 and A100), with 1σ levels shown by dashed curves. The inset depicts the part of the main plot indicated in the lower left corner (solid rectangle). The vertical dashed line at $S = 0.19$ represents the maximum of the annually averaged solar S-index observed until now. The solid and long-dashed horizontal lines mark the maximum and the mean variability in the solar-like sample of R20, respectively. Note that the calculations are performed for stars observed from their equatorial planes; thus they represent upper limits of the rotational variability.

value can be reached, using Figure 3. For the solar level of nesting (F50) an activity level of $S = 0.25$ is needed. According to Equations (1)–(2) from Shapiro et al. (2014) employed in our model (see Section 2), such an S-index corresponds to mean spot and facular coverages of about 17 and 5 times larger than the corresponding annually averaged solar values during the maximum of Cycle 22. For F100 (a single nest throughout four years), the variability $R_{90} = 0.7\%$ is reached already at $S \simeq 0.215$ (spot and facular coverages are about 6 and 2 times higher than solar, respectively). For F90 the same level is reached at $S \simeq 0.23$ (spot and facular coverages 10 and 3 times solar).

In the active-longitude mode, $R_{90} = 0.7\%$ is reached for A50 at $S \simeq 0.23$, similar to F90. For A90, $S \simeq 0.22$ would be sufficient (spot and facular coverages 7 and 2.5 times solar, respectively). The significant difference between the extreme cases F100 and A100 is because in free nesting F100 forms a single nest, whereas A100 distributes the same number of emergences into two ALs in opposition, resulting in weaker variability.

3.2. Active Longitudes: More Regular Light Curves

We now investigate the impact of nesting on the morphology of light curves. Figure 4 shows sample light curves, for $S \simeq 0.19$ (expected during a solar maximum) and $S \simeq 0.23$. In the free-nest mode, the variability increases with the nesting degree (in line with Figure 3), but the brightness variation is still far from being sinusoidal, even for F90. In the active-longitude mode at $S = 0.23$, the light curves not only reach the highest observed variability levels, but also become much more regular. They look very similar to the light curves shown by many periodic stars, i.e., sine-like, exhibiting smooth changes between consecutive dips. Additional simulations involving a single AL with the same width resulted in stronger but less sinusoidal rotational modulations.

4. Discussion and Conclusions

Data collected by the Kepler space telescope indicate that stars with near-solar rotation rates and fundamental parameters can have a broad range of photometric variabilities. R20 have recently found that the periodic subsample of such stars appears to be significantly more variable than the Sun.

We have shown here that the full range of observed variabilities of such stars can be explained by preserving solar properties of active regions but going well beyond the degree of active-region nesting presently observed on the Sun and somewhat beyond the solar magnetic activity level. This is accomplished using a very simple model, in which the fundamental properties of solar variability are reasonably well represented, though for other stars some of the assumptions involved may not apply.

Our model allows connecting the difference between the rotational variability of pseudosolar and solar-like samples of R20 with the differences in the activity level. We have shown here that the exact connection depends on the degree of AR nesting. Our calculations indicate that the mean and maximum variability amplitudes of the solar-like sample analyzed by R20 (R_{90} being 0.38% and 0.70%, respectively) can be obtained by a simple increase of activity from the solar value (i.e., without increase of nesting). This, however, would require an increase of the activity level up to $S = 0.22$ for the mean and $S = 0.25$ for the maximum. With AR nesting, say, the F90 case (compared to F50 for the Sun), we need a much more moderate increase of activity, $S \simeq 0.20$ (mean) and $S \simeq 0.23$ (maximum).

Both estimates appear to be consistent with the recent results from Zhang et al. (2020, see their Figure 1), who utilized LAMOST spectra to measure S-indices of stars from the R20 sample and showed that the periodic, "solar-like" stars are moderately more active than the Sun. Unfortunately, we cannot make a direct comparison of the S-indices found by Zhang et al. (2020) with our numerical experiments, because the LAMOST
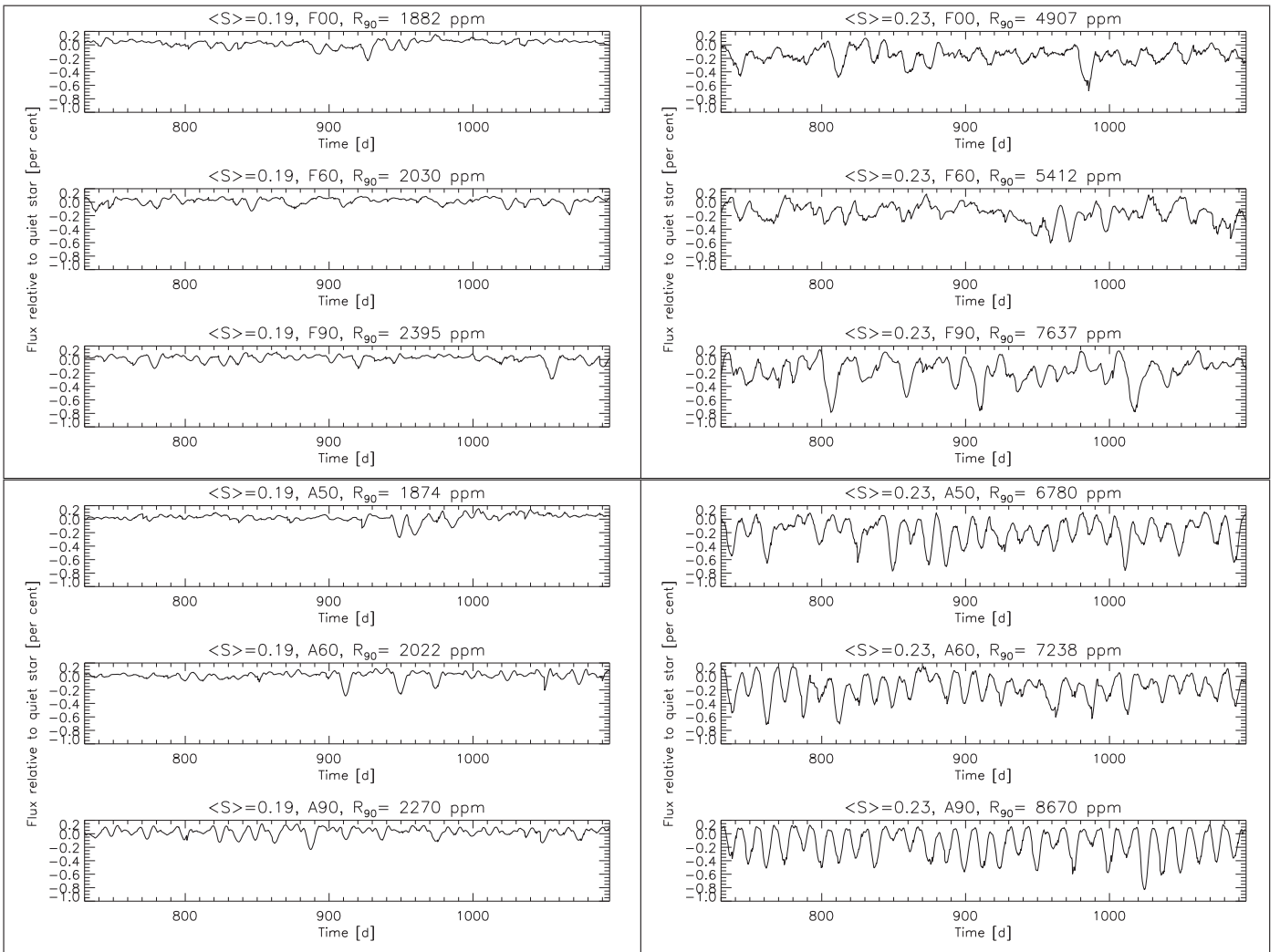
Figure 4. Sample light curves for free-nesting (upper panels) and active-longitude (lower panels) modes. For each mode, two activity levels (columns) are shown with three degrees of nesting each (rows). $S \simeq 0.19$ in the left panels, and $S \simeq 0.23$ in the right panels. The nesting mode and degree, and the 25 day variation amplitude, R_{90}, are indicated above each panel. Note that for $S = 0.19$ the slightly higher R_{90} of case F90 compared to A90 is a mere coincidence and does not contradict the overall trend of the AL mode yielding higher variability than free-nest mode (see Figure 3).

S-index scale cannot be directly converted to the Mount-Wilson (MW) S-index used in our study. At the same time, Figure 1 from Zhang et al. (2020) shows that the mean S-index of the solar-like stars is lower than that of stars with rotation periods between 10 and 20 days. These faster-rotating stars are expected to have S-indices (in MW scale) between about 0.20 and 0.28 (see Figures 1–2 from Shapiro et al. 2020b).

Furthermore, we found that the nearly sinusoidal light curves of strongly variable solar-like stars can be reproduced by a highly nonaxisymmetric pattern of AR emergence, with an azimuthal wavenumber of 2. Consequently, such a pattern of AR emergence can simultaneously explain both the amplitude and morphology of the observed light curves. We note that double active longitudes have often been suggested to explain the light curves of very active BY Dra-, RS CVn-, and FK Com-type cool stars (Berdyugina 2005). Most such stars are components of close binaries.

We suggest three possible mechanisms for solar-like stars to exhibit active longitudes: (1) they can be components of non-eclipsing close binaries or they have warm or hot gas-giant components (Shibata et al. 2013). In the active components of such systems, tidal forces can lead to preferred longitudinal zones for emerging flux tubes (see, e.g., Holzwarth & Schüssler 2003, though they found this tendency for $P_{\rm rot} \sim 2$ d). In that case, AL-type nesting can permanently lead to strong rotational variability (see also Korhonen & Elstner 2005). (2) AL-type nesting can be a generic phenomenon, which all solar-type stars can undergo from time to time, or above some activity level. (3) Solar-like stars can have a time-varying degree of nesting, as well as temporarily existing ALs, which can be responsible for those light curves exhibiting transitions between very regular and less regular variations. These possibilities should be explored more thoroughly in the future.

The model presented in this Letter was kept very simple, to demonstrate the overall effects of AR nesting on brightness variability in solar-like stars. Physically more consistent models that simulate flux emergence and surface transport processes (following Işık et al. 2018) including effects of AR nesting and the rotation rate are planned for a subsequent study.
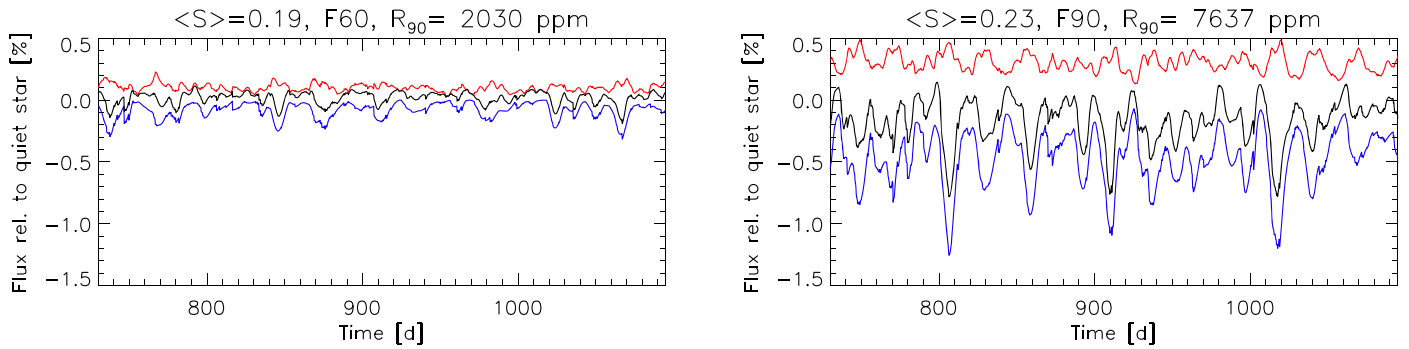
Figure 5. Light curves (black) decomposed into facular (red) and spot (blue) components, for free-nesting mode. Left panel: low-activity, low-nesting ($S = 0.19$, F60 case); right panel: high-activity, high-nesting ($S = 0.23$, F90 case). The facular-to-spot area ratios during AR emergence are 2.92 and 1.43 for $S = 0.19$ and $S = 0.23$, respectively (see the text of the Appendix for details on how it is calculated).

Appendix
Forward Modeling of Light Curves

The detailed procedure of light-curve synthesis has been described by Shapiro et al. (2020a). We briefly explain in the following the main concept of the model relevant to our purpose of simulating rotational variability.

In our model active regions (ARs) emerge instantaneously at random times within 1600 days. Consequently, the emergence frequency of ARs is constant, i.e., we do not consider stellar activity cycles. The activity level of a simulated star is then defined by the total number of emergences. For each realization of emergences we calculate not only the time series of stellar brightness, but also the time series of disk-area coverage by spots. Using the dependence between the stellar disk coverage by spots and the S-index extrapolated by Shapiro et al. (2014) from the Sun to more active stars, we obtain S corresponding to a given light curve.

The ARs in our model consist of spot umbrae, spot penumbrae, and faculae. The contrast of a particular magnetic feature relative to the quiet regions (i.e., regions on the stellar surface free from any apparent manifestation of magnetic features) depends on the wavelength and the position of the magnetic feature on the stellar disk. We have used wavelength-dependent contrasts calculated by Unruh et al. (1999) and convolved them with the Kepler spectral passband (see Nèmec et al. 2020 for a comprehensive study of the effect of different passbands on the measured variability).

The areas of the spot parts of ARs are randomly drawn from a log-normal probability distribution, which considers spot groups at their maximum-development phase, given by Baumann & Solanki (2005, Table 1). We choose areas to fall between 60 and 3000 μSH (millionths of a solar hemisphere), to cover the entire range of sunspot group areas in the part of the Royal Greenwich Observatory (RGO) record for which the distribution can be fit by a log-normal function. Following Wenzler et al. (2006) we attribute 80% of spot area to penumbra and the remaining 20% to umbra. The ratio between facular and spot areas of ARs at the moment of emergence,

Table 1
Model Parameters

Parameter	Value
Equatorial rotation period	25 days
Axial inclination	90°
Spot area distribution	Log-normal[a]
Spot area range	$60 < A_s < 3000\ \mu$SH
Spot decay law	Linear; 25 μSH days^{-1}
Facula-spot lifetime ratio	$\tau_f/\tau_s = 3$

Notes.
[a] Bogdan et al. (1988); Baumann & Solanki (2005).

A_f/A_s, is assumed to be the same for all ARs for a given stellar activity level (see Figure 10 from Shapiro et al. 2020a). It is calculated to fulfill the relationship between the instantaneous facular and spot disk-area coverages observed for the Sun and extrapolated to more active stars (namely, Equations (1)–(2) from Shapiro et al. 2014).

We do not consider a specific geometrical shape for an AR, prescribing the same value of the foreshortening to the entire region. This approximation is justified by the fact that the detailed morphology of ARs (i.e., spot group surrounded by facular regions) has a small effect on rotational variability, as long as the ARs are in the same size range with solar ARs, which we assume here for other solar-like stars.

Following the emergence, we model the decay of spots and faculae as a continuous reduction of their areas. We consider a linear decay law following an instantaneous emergence, with a spot decay rate of 25 μSH days^{-1}, given that quadratic and linear decay laws are not distinguishable in the RGO data set (Baumann & Solanki 2005). For a given active region a decay time of its facular part was set to be 3 times longer than those of its spot part (see Shapiro et al. 2020a for a detailed discussion and case study).

The input physical parameters determining the final light curve are listed in Table 1.

Two example light curves are shown in Figure 5 (taken from Figure 4), in which the spot and facular components are shown separately. The facular-to-spot area ratio during the emergence of any spot is determined by the S-index, such that the ratio decreases with S (see above). As a result, the relative contribution of the spot component in the total variability increases with the activity level.

ORCID iDs

Emre Işık ⬤ https://orcid.org/0000-0001-6163-0653
Alexander I. Shapiro ⬤ https://orcid.org/0000-0002-8842-5403
Sami K. Solanki ⬤ https://orcid.org/0000-0002-3418-8449
Natalie A. Krivova ⬤ https://orcid.org/0000-0002-1377-3067

References

Aigrain, S., Llama, J., Ceillier, T., et al. 2015, MNRAS, 450, 3211
Amazo-Gómez, E. M., Shapiro, A. I., Solanki, S. K., et al. 2020, A&A, 636, A69
Basri, G., Walkowicz, L. M., & Reiners, A. 2013, ApJ, 769, 37
Baumann, I., & Solanki, S. K. 2005, A&A, 443, 1061
Berdyugina, S. V. 2005, LRSP, 2, 8
Bogdan, T. J., Gilman, P. A., Lerche, I., & Howard, R. 1988, ApJ, 327, 451
Brouwer, M. P., & Zwaan, C. 1990, SoPh, 129, 221
Castenmiller, M. J. M., Zwaan, C., & van der Zalm, E. B. J. 1986, SoPh, 105, 237
Gaizauskas, V., Harvey, K. L., Harvey, J. W., & Zwaan, C. 1983, ApJ, 265, 1056
Holzwarth, V., & Schüssler, M. 2003, A&A, 405, 303

Işık, E., Solanki, S. K., Krivova, N. A., & Shapiro, A. I. 2018, A&A, 620, A177
Korhonen, H., & Elstner, D. 2005, A&A, 440, 1161
McQuillan, A., Mazeh, T., & Aigrain, S. 2014, ApJS, 211, 24
Nèmec, N. E., Işık, E., Shapiro, A. I., et al. 2020, A&A, 638, A56
Özavcı, I., Şenavcı, H. V., Işık, E., et al. 2018, MNRAS, 474, 5534
Pojoga, S., & Cudnik, B. 2002, SoPh, 208, 17
Reinhold, T., Reiners, A., & Basri, G. 2013, A&A, 560, A4
Reinhold, T., Shapiro, A. I., Solanki, S. K., et al. 2020, Sci, 368, 518
Shapiro, A. I., Amazo-Gómez, E. M., Krivova, N. A., & Solanki, S. K. 2020a, A&A, 633, A32
Shapiro, A. V., Shapiro, A. I., Gizon, L., Krivova, N. A., & Solanki, S. K. 2020b, A&A, 636, A83
Shapiro, A. I., Solanki, S. K., Krivova, N. A., et al. 2014, A&A, 569, A38
Shibata, K., Isobe, H., Hillier, A., et al. 2013, PASJ, 65, 49
Snodgrass, H. B. 1983, ApJ, 270, 288
Unruh, Y. C., Solanki, S. K., & Fligge, M. 1999, A&A, 345, 635
Usoskin, I. G., Berdyugina, S. V., & Poutanen, J. 2005, A&A, 441, 347
Walkowicz, L. M., & Basri, G. S. 2013, MNRAS, 436, 1883
Wenzler, T., Solanki, S. K., Krivova, N. A., & Fröhlich, C. 2006, A&A, 460, 583
Witzke, V., Reinhold, T., Shapiro, A. I., Krivova, N. A., & Solanki, S. K. 2020, A&A, 634, L9
Zhang, J., Shapiro, A. I., Bi, S., et al. 2020, ApJL, 894, L11